

Chromospheric Carbon Monoxide Formation around a Solar Pore

JOHNATHAN R. STAUFFER,¹ KEVIN P. REARDON,^{2,1} AND MATT PENN³

¹Department of Astrophysical and Planetary Sciences, 391 UCB, 2000 Colorado Ave, Boulder, CO 80309, USA

²National Solar Observatory, 3665 Discovery Dr, Boulder, CO 80303, USA

³Raytheon Technologies, 1151 E Hermans Rd, Tucson, AZ 85756, USA

ABSTRACT

We present the first coordinated observations of the fundamental ($\Delta\nu = 1$) ro-vibrational band of carbon monoxide (CO) and three visible/IR atomic lines (Na I 5896 Å, Fe I 7090 Å, and Ca II 8542 Å) sensitive to the upper photosphere and chromosphere. Observations of NOAA AR 11159 on February 14, 2011 revealed several long-lived cooling events (“cold bubbles”) occurred primarily at the boundary of a large pore (the decaying remains of the leading spot in the active region). These events were not visible in the three atomic lines. These events showed self-similar temporal evolution, with timescales consistent with CO chemical formation timescales in the low chromosphere. Due to the lack of such features in the quiet Sun, we hypothesize that the magnetic canopy field surrounding the pore in the chromosphere, which suppresses the upward propagation of high-frequency acoustic waves from the photosphere and subsequent formation of shocks, depresses the acoustic heating of the atmosphere surrounding the pore and allows for CO to condense and cool the atmosphere at chromospheric heights.

1. INTRODUCTION

The *chromosphere* is an area of immense importance to our understanding of the solar atmosphere. While the lower-lying *photosphere* is primarily dominated by hydrodynamics and the diffuse *corona* by magnetic forces, these effects are comparable in magnitude in the chromosphere. This means that energy passing through it from below can be reflected, redirected, or converted between different wave modes that can then be dissipated locally or transmitted higher into the corona. Since the Sun’s extremely high coronal temperatures are thought to be sustained by an influx of energy from the photosphere, a thorough understanding of the chromosphere and how it mediates and transforms this energy flux is necessary to understand coronal heating.

However the chromosphere is also notoriously difficult to study. Because of complex interactions between the magnetohydrodynamic forces in the region, observations of chromospheric structures (such as the elongated *fibrils* that surround photospheric magnetic field concentrations) can be interpreted neither as purely hydrodynamic phenomena nor as straightforward representations of the chromospheric magnetic field. Furthermore, the chromosphere’s low density compared to the photosphere means that atomic line transitions are dependent not only on local plasma conditions (such as temperature and density), but also the solar radiation field – hence, the responses of most spectral lines that form in the chromosphere are dominated by non-local thermodynamic equilibrium (NLTE) effects.

Despite these difficulties, careful studies of the chromosphere using spectral diagnostics ranging from the near-infrared to the ultraviolet have established a canonical view of the chromosphere as a “plateau” of elevated ($\sim 6000 - 10\,000$ K) temperature, bounded from below by a *temperature minimum* (T_{min}) of ~ 4400 K at $z \approx 500$ km (measured relative to the $\tau_{500} = 1$ surface in the 500 nm continuum) and from above by a steep temperature gradient marking the *transition region* to the solar corona at $z \approx 2000$ km¹. However, certain features of the solar spectrum shed doubt on this model of a ubiquitously hot chromosphere. Early measurements of the fundamental ($\Delta\nu = 1$) molecular band of carbon monoxide (CO) by Noyes & Hall (1972) showed unexpectedly cool ($T \approx 3500$ K) line core temperatures at the extreme Solar limb – a phenomenon then attributed to emission from cool granular downflow lanes. However, later observations Ayres & Testerman (1981) found that the limb-darkening behavior of these lines – which range in temperature from ~ 4000 K near disk-center to as low as 3700 K at the extreme limb – were better explained by the elimination of the traditional chromospheric temperature rise at $z \approx 500$ km. This conclusion was bolstered by measurements of the CO

¹ Models which aim to describe different components of the solar atmosphere, such as the various models given in Fontenla et al. (1993), differ slightly in their description of the chromosphere – mainly in its average temperature and the height of the transition region – but are qualitatively very similar

lines' limb emission, which show significant amounts of CO at as far as ~ 1000 km above the solar surface (Solanki et al. 1994). Combined, these observations suggest that cool, sub-4000 K gas extends beyond the “temperature minimum” and into the lower layers of the chromosphere, which should be too hot to sustain significant amounts of CO according to traditional models.

Several models of CO formation in the solar atmosphere have been developed in order to explain these results. Most straightforward is the static “COmosphere” approach (e.g. Ayres et al. 2006), which posits that the low chromosphere (described by classical “hot” models) is permeated by cool, CO-rich “clouds” (described by a “cold” model featuring an extended temperature minimum, needed to reproduce the CO line core intensities and limb extensions). Such approaches yield a two-peaked contribution function for many of the CO spectral lines, indicating that their intensities are determined both by the conditions in the upper photosphere and the chromosphere – at disk-center, this contribution is approximately equal, while near the limb it shifts to depend primarily on the chromospheric temperature due to the increased line opacity along the inclined line-of-sight. However, while the “COmosphere” model is capable of reproducing the average solar spectrum, it predicts the existence of small-scale ($\lesssim 0.4''$), ultra-cold “dark points”, which are not seen at the resolution of current IR spectrographs (Ayres 2003). While the existence of such features is not impossible, there is no theory of how they remain un-mixed with the remaining “hot” chromosphere.

Alternatively, high-altitude CO can be created dynamically in the wake of large-amplitude acoustic waves in the solar atmosphere (Carlsson & Stein 1995, 1997, a “part-time COmosphere”, for example the 1-D models proposed by). In this model, the chromospheric temperature varies dramatically with the passage of these waves, but its cold “average” temperature of the atmosphere allows it to reproduce the CO brightness temperatures and limb extensions. However, these models were criticized for their unrealistic predictions for other chromospheric diagnostics such as Lyman- α (Kalkofen 2001). Furthermore, early 2-D (Wedemeyer-Böhm & Steffen 2007) and 3-D (Wedemeyer-Böhm et al. 2006) hydrodynamic modelling of CO formation using the CO5BOLD simulation code (which can account for time dependent, non-equilibrium CO chemistry) indicated that the acoustic heating in the non-magnetic chromosphere is too high for significant CO to form above photospheric heights. Further confusing things, recent simulations (Leenaarts et al. 2011) using the Bifrost code (Gudiksen et al. 2011, which incorporates more sophisticated chromospheric physics than CO5BOLD, such as non-LTE hydrogen ionization, but not atmospheric chemistry), have instead indicated that cool (< 2000 K) pockets of gas can indeed form in the non-magnetic chromosphere in the wake of acoustic shocks, although the authors did not model how these cooling episodes might influence chromospheric CO and its associated radiative cooling effects.

A thorough understanding of these lines and their sensitivity to the chromospheric temperature is more important now than ever, given the development of two cutting-edge IR solar spectrographs. First, the new CrYogenic spectRogrAph at the Goode Solar Telescope (GST/CYRA, Yang et al. 2020) will be capable of observing these lines at a $\sim 0.7''$ spatial resolution with a spectral resolution of $R \approx 1.67 \times 10^5$, enough to fully resolve the cores of the CO lines (see Ayres 2003) – a feat previously achievable only through (spatially unresolved) Fourier transform spectroscopy. Construction of CYRA is nearly complete, and preliminary observations of the CO $4.7\text{ }\mu\text{m}$ band have been presented (Yang et al. 2020; Li et al. 2020). Additionally, the Cryogenic Near-InfraRed SpectroPolarimeter at the Daniel K. Inouye Solar Telescope (DKIST/Cryo-NIRSP, Fehlmann et al. 2016) will be capable of observing the CO spectrum at a spatial resolution of $\sim 0.3''$ and spectral resolution of $R \equiv \lambda/\Delta\lambda \approx 1.1 \times 10^5$: more than twice the spatial and spectral resolution of the previous generation of solar IR spectrographs (such as the one at the now-decommissioned McMath Pierce Solar Telescope). This high resolution instrument, combined with the excellent seeing characteristics of its observing site on Haleakalā, will provide an unprecedented view of the Sun at $4.7\text{ }\mu\text{m}$. However, it is likely that better observation of these lines will not be enough to resolve the controversies surrounding solar CO; instead, we will need to rely on multi-wavelength observations to provide additional context to the CO lines in order to resolve the mysteries surrounding their formation. By choosing an ensemble of spectral lines with complementary regions of sensitivity, one can construct a holistic view of the behavior of the solar atmosphere beyond what any single line can provide. This additional context is especially important when studying lines with uncertain or ambiguous line formation characteristics, such as the CO fundamental band – by carefully selecting complementary spectral diagnostics with overlapping regions of sensitivity, the ambiguity surrounding those lines' formation can be reduced. This paper marks one of the first such studies, combining wide-field observations of the CO fundamental band with high-resolution imaging spectrograph data of several atomic lines.

2. OBSERVATIONS

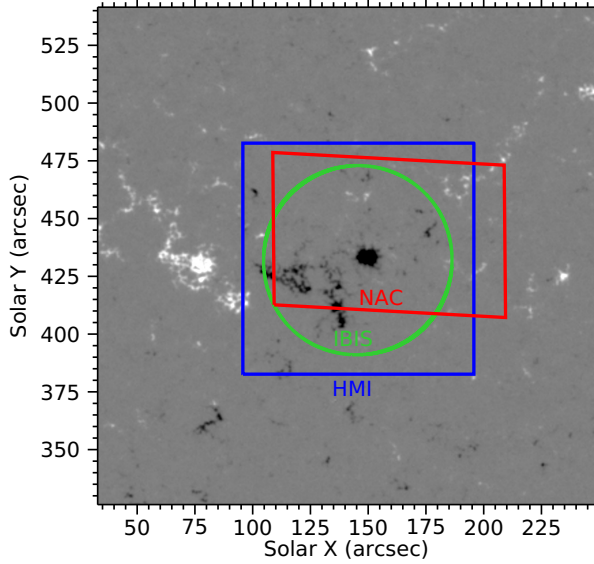


Figure 1. The approximate locations of the three instruments’ fields of view, superimposed on the HMI magnetogram. The green circle represents the $\sim 80''$ aperture of IBIS, while the red rectangle shows the region covered by the McMP/NAC scan (the slit is oriented north/south and scans from east to west). For reference and coalignment, a $100''$ cutout from SDO/HMI (blue square) was extracted to cover the full IBIS FOV and its region of overlap with McMP/NAC.

In this paper, we present observations of NOAA Active Region 11159 coordinated between the Dunn Solar Telescope (DST) and McMath-Pierce Solar Telescope (McMP) on February 14, 2011. At the DST, the Interferometric BIdimensional Spectropolarimeter (IBIS; Cavallini 2006; Reardon & Cavallini 2008) and Facility InfraRed Spectrometer (FIRS, Jaeggli et al. 2010) were used to observe the target region². At the McMP, the NSO Array Camera (NAC, Ayres et al. 2008) was used with the infrared spectrograph to observe the same region in the mid-infrared. Context images in the white-light continuum and photospheric magnetic field maps were provided by the Helioseismic and Magnetic Imager onboard the Solar Dynamics Observatory (SDO/HMI Pesnell et al. 2012; Scherrer et al. 2011).

Figure 1 shows AR 11159 at the time of observation, as well as the approximate fields of view of the IBIS (green) and NAC (red) instruments. Additionally, a $100''$ square HMI cutout (used as a stable spatial reference) is marked in blue. The observations are roughly centered on a large magnetic pore (the decaying remains of the leading spot) which served as the AO lock point for IBIS (the trailing spot has already decayed and lies to the east of the field-of-view). The pore was located 9° west and 20° north of disk-center the time of our observations ($\mu = 0.91$, or $\theta = 22^\circ$).

2.1. McMP Observations

NAC observed AR 11159 from 17:08:47 UT to 19:03:50 UT in the $4.7\text{ }\mu\text{m}$ molecular band of CO. The spectral window was centered on the line corresponding to the 3-2 R 14 ro-vibrational transition at 4667 nm , a strong line which is minimally blended with telluric lines and other strong CO features. The slit covers $55''$ in the north-south direction with a sampling of $0.064''\text{ px}^{-1}$, and was scanned across the region from east to west with an approximately $1''$ step size. To match this spatial under-sampling in the scan direction and because seeing conditions limited the telescope’s resolution, we binned the NAC spectra by 16 pixels along the slit (yielding a $1''$ sampling), decreasing the relative noise of the CO spectrum by a factor of 4. Each slit pointing required an integration time of 0.5 s , and a full 112-step scan was completed with a cadence of $\sim 58\text{ s}$.

We applied dark and flat corrections to the NAC spectra, and corrected them for rotation with respect to the detector axes and time-dependent shifts in the dispersion direction. The flat-field collected by the telescope operators was constructed by fixing the telescope onto a region of quiet Sun and scanning through the IR spectrum. This has the benefit of removing spectral features from the flat field, but results in an imperfect correction due to the flat-field being collected over a different wavelength range than the observed spectra. To correct for this, a second-order “spatial

² Here, we only focus on the IBIS data.

flat” was constructed by removing the average solar spectrum from the average quiet-Sun spectrum observed near the western edge of the scan. A similar correction was made to account for slight shifts in the flat field over the course of the observing run.

2.2. DST/IBIS Observations

IBIS observed AR 11159 in two observing sequences: first from 17:11:14 UT to 17:15:43 UT (consisting of 13 spectral scans), and then from 17:23:17 UT to 19:01:07 UT (281 scans). Due to unstable seeing in the first observing sequence and at the end of the second sequence, we use only the first 236 scans of the second observing run, spanning from 17:23:17 UT to 18:45:15 UT (approximately 80 minutes of continuous observations).

The instrument sequentially captured scans of Na I 5896 Å (D1; 31 wavelength points), Fe I 7090 Å (20 wavelength points), and Ca II 8542 Å (31 wavelength points). Each scan step took a total integration time of ~ 0.2 sec. Accounting for a ~ 1.4 sec delay to change between prefilters for the different lines, the set of three spectral lines was observed with a cadence of ~ 21 s. IBIS was operated in spectroscopic mode (without polarimetry).

We applied dark, flat-field, instrumental blueshift, and fringe-removal corrections to the IBIS data. Additionally, seeing-induced distortions were removed by “de-stretching” the images such that they align with the closest-in-time HMI continuum image, which provides a stable reference of the solar granulation. After this transformation, the IBIS data have a uniform sampling of 0.1 ″/px. Lastly, corrections for scattered light contamination and attenuation by the spectral pre-filter were performed by comparing the average quiet Sun spectra to the NSO Fourier Transform Spectrometer (FTS) atlas (Kurucz et al. 1984). This calibration also provides an absolute wavelength scale for each of the scanned lines, as well as a relative intensity scale.

2.3. Coalignment

The NAC scans were co-aligned with the IBIS images by comparing the positions of the pore and several magnetic network elements, which appear clearly as bright features in maps of both the CO and Fe I 7090 Å line-core intensities observed by IBIS (see Section 2.2). A linear regression between the coordinates of these features in the IBIS and NAC reference frames yields an affine transformation that can be used to transform NAC scans into the IBIS frame, and vice versa.

3. METHODS

3.1. Spectral Line Parameters

For ease of comparison between the four spectral diagnostics (Na I D1, Fe I, Ca II, and CO), we calculated a set of standard line parameters. The line core intensity I_0 and Doppler shift v_D were extracted for each line by fitting a parabola to their cores. For the CO line (which does not show appreciable asymmetry at the spectral resolution of the McMP spectrograph), a center-of-gravity measurement of the Doppler velocity is used instead to minimize uncertainty in the measurement:

$$v_D^{cog} = \int_{\lambda_-}^{\lambda_+} \left(1 - \frac{I_\lambda}{I_c}\right) \lambda d\lambda \quad (1)$$

where I_λ is the spectral line profile and I_c is the local continuum intensity (here, λ_- and λ_+ represent points in the local continuum just outside the absorption line – as long as they don’t lie in another solar or telluric line, their precise position does not matter). These parameters give information about the temperature and line-of-sight velocity in the solar atmosphere. Additionally, the equivalent width of the CO line was calculated:

$$W_\lambda = \int_{\lambda_-}^{\lambda_+} \left(1 - \frac{I_\lambda}{I_c}\right) d\lambda \quad (2)$$

The equivalent width of a spectral line is a monotonic function of the column density of absorbers in the solar atmosphere. In the absence of a precise theoretical model for this dependence (the *curve of growth*, the calculation of which is beyond the scope of this paper), we treat W_λ as a qualitative proxy for the column density of CO in the atmosphere. While several CO lines are captured within the NAC spectral range, we focus here only on the 3-2 R 14 transition, which is minimally blended with telluric and other CO lines, and the most evenly illuminated across the field-of-view.

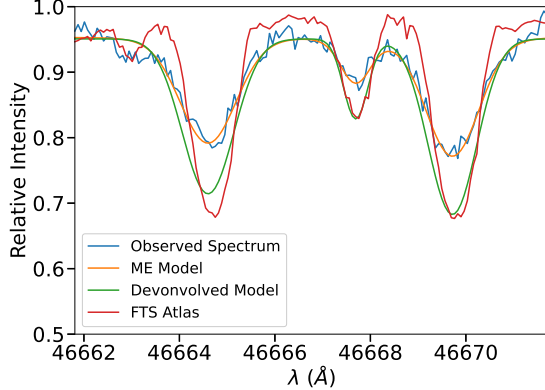


Figure 2. Results of the Milne-Eddington inversions of the CO spectra. The observed spectra are shown in blue, while the modeled spectrum are shown in orange. The green line shows the model spectrum with the line spread function of the telescope removed, as well as a constant stray light background. The FTS atlas is shown in red for reference.

3.2. Milne-Eddington Inversion of the CO Lines

Because the CO lines form in LTE (Ayres & Wiedemann 1989), their core intensities can be interpreted in terms of *brightness temperatures* (T_b) that reflect the gas temperature of the solar atmosphere at their heights of formation. However, because the CO lines are so narrow their line core intensities are heavily influenced by the line spread function (LSF) of the McMath Pierce spectrograph (which has insufficient spectral resolution to resolve the narrow CO lines, see Ayres 2003) and scattered light. To account for these effects, we modeled the 3-2 R 14 line (as well as the nearby 4-3 R 23 and 7-6 R 67 lines) using a Milne-Eddington model:

$$I_\lambda = S_0 + \frac{S_1}{1 + \eta_1\phi_1(\lambda) + \eta_2\phi_2(\lambda) + \eta_3\phi_3(\lambda)} \quad (3)$$

$S = S_0 + S_1\tau$ defines the source function of the solar atmosphere, η_i are the line strengths, and $\phi_i(\lambda)$ are Gaussian absorption profiles. The ME model was convolved with the empirical LSF of the McMath-Pierce spectrograph (Ayres 2003) for direct comparison with the observed spectral profiles. Once an optimal model fit was found, the model profile was de-convolved with the LSF, and a constant scattered-light background was subtracted such that the depth ratio of the 3-2 R 14 and 7-6 R 67 lines matches the FTS IR atlas (Livingston & Wallace 1991). The absolute scale of these brightness temperatures is determined by assuming the continuum intensity to be the disk-center average brightness temperature of the $4.7\text{ }\mu\text{m}$ continuum, as an independent calibration of the temperature is not available for these observations. The observed and corrected spectra are shown in Figure 2.

4. RESULTS

4.1. Comparison of Line Core Intensities

By comparing the appearance of the solar surface as seen in the CO with the other spectral diagnostics (which have well understood formation characteristics), we can begin to piece together an understanding of the sensitivity of these lines to various regions of the atmosphere. Figure 3 shows a representative example of the line core intensity of these spectral lines, as well as the visible continuum and HMI magnetogram.

Of all the lines observed by IBIS, Fe I 7090 Å forms the lowest, with its line core sensitive to the mid-photosphere. Therefore, its line core intensity is dominated by inverse granulation (dark granules separated by bright inter-granular lanes, caused by cooling from adiabatic expansion above the granular convective cells and the corresponding heating above the downflow lanes) and the 5-minute helioseismic oscillations. The plage and magnetic network appear bright (due to the higher magnetic pressure in these areas of concentrated field, which results in a lower density to maintain hydrostatic equilibrium and lowers the height of line formation), while the pore is dark due to the suppression of the solar convection by its strong magnetic field.

The formation of Na I D1 is more complicated, as its line core intensity is dominated by (NLTE) resonance scattering (Leenaarts et al. 2010). This causes the line core to be sensitive to a wide range of heights spanning the photosphere

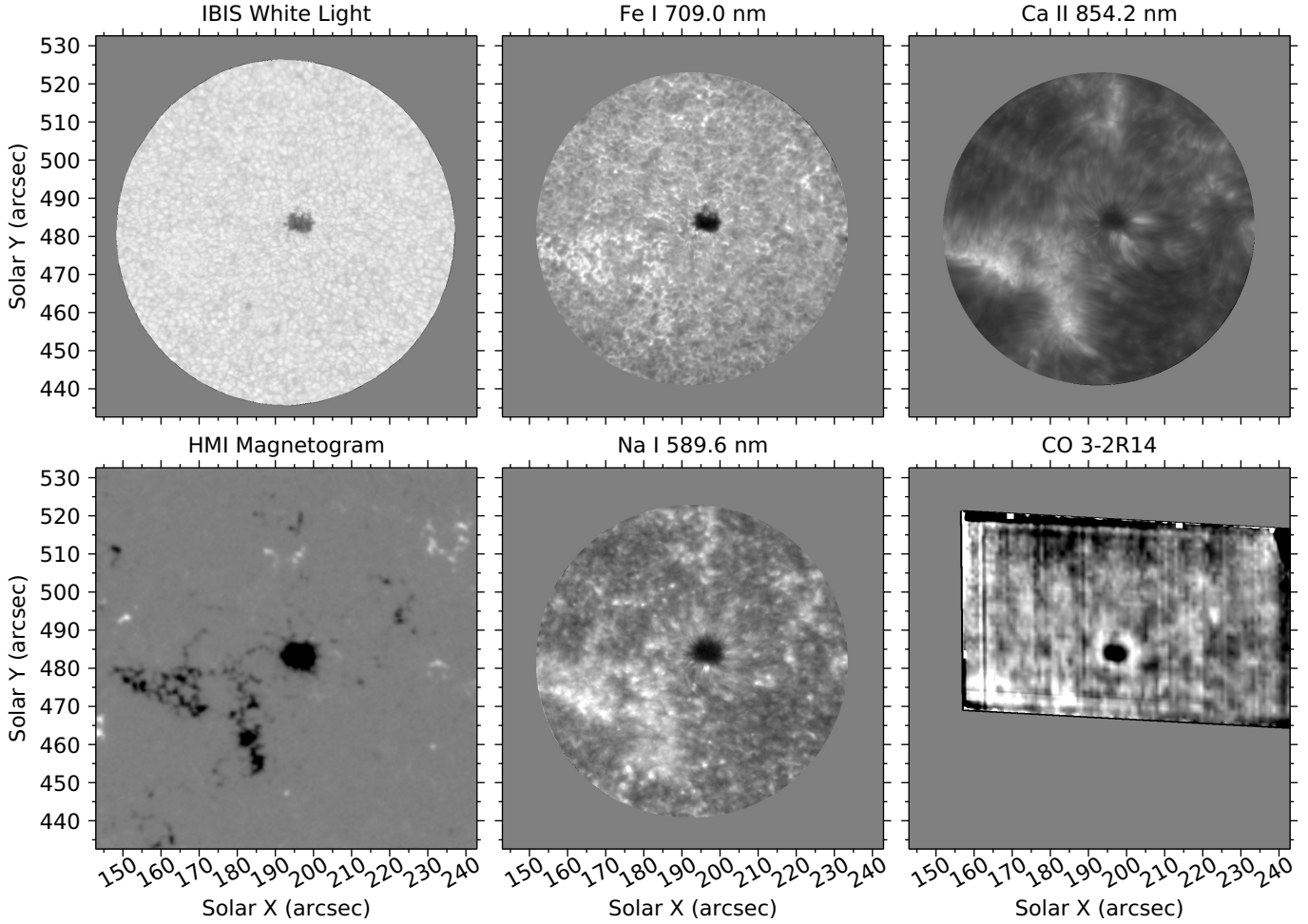


Figure 3. Comparison of the line core intensities in the four observed spectral diagnostics. The left two panels show the IBIS white light reference (*top*) and HMI magnetogram (*bottom*). The line core intensities are shown for the photospheric Fe I and Na I lines (middle panels), and for the chromospheric Ca II line and the CO 3-2 R 14 line (right panels), the latter of which forms in the temperature minimum. The IBIS scan shown here was captured between 17:35:46 UTC and 17:36:06 UTC, while the CO scan was captured between 17:34:54 UTC and 17:35:49 UTC.

and lower chromosphere. The line-core intensity images appear similar to those of Fe I 7090 Å, with a few notable differences. First, faint, elongated “penumbra-like” filaments appear around the edge of the pore, due to the increased influence of the magnetic field on the plasma at its higher (average) formation height. We also note that the bright spots corresponding to the plage and network are more diffuse than in Fe I; this is due to 3-D scattering effects redirecting light emitted horizontally from their hotter, magnetized atmospheres into the line-of-sight (for further discussion, see e.g. Leenaarts et al. 2010), creating bright, diffuse “aureoles” surrounding these features.

The highest-forming line observed by IBIS is Ca II 8542 Å. This line is sensitive to two regions: the shallow, LTE-dominated wings are sensitive to the mid-photosphere, while the NLTE line core is sensitive to chromospheric heights (for more detailed discussion, see Cauzzi et al. 2008). Because of this, the line-core intensity maps are dominated by elongated *fibrils* surrounding the pore and plage, which are the result of plasma being partially shaped by the inclined chromospheric *canopy field* in those regions. Where the photospheric magnetic field is concentrated, fibrils are mostly absent and the intensity is brighter and fairly uniform, typically indicating higher chromospheric temperatures.

The CO line-core intensity is comparatively uniform, with no large scale structures (e.g. fibrils) visible at the $\sim 1''$ sampling of the NAC observations, with the exception of the dark pore and bright plage/network³. Additionally, we

³ We note that observations taken at the McMP under ideal seeing conditions (e.g., Uitenbroek 2000) show clear inverse granulation, similar to that seen in the photospheric Fe I 7090 Å line.

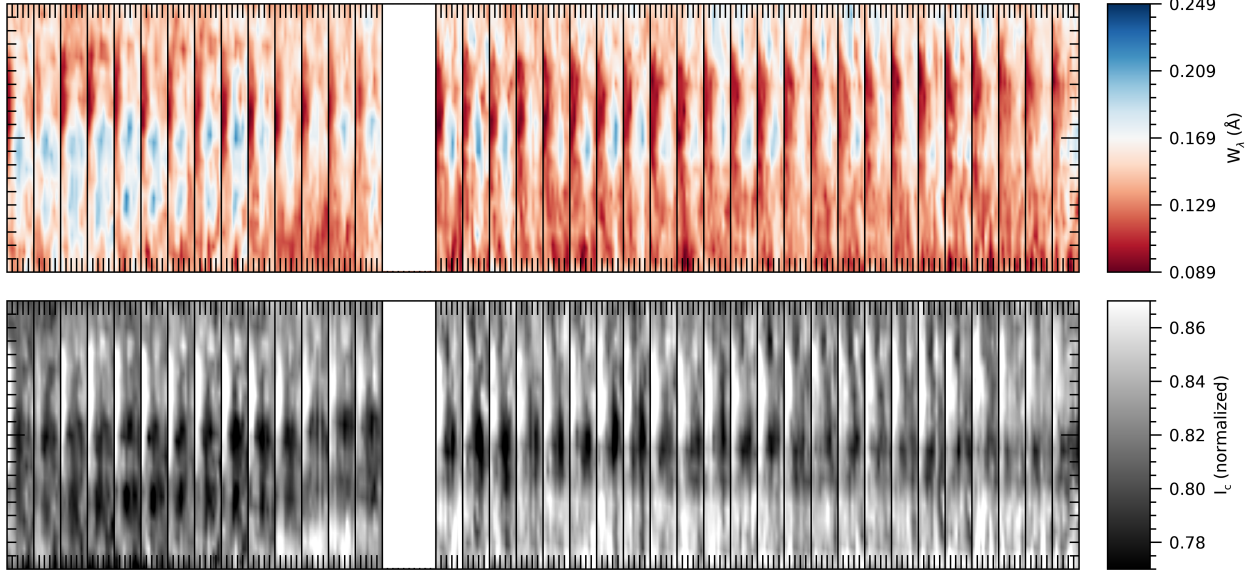


Figure 4. A space-time diagram showing both the equivalent width (top) and the line core intensity (bottom) of an anomalous absorption feature (termed a “cold bubble”) found to the southwest of the pore. The ticks on the x -axis represent $2''$ intervals, while the ticks on the y -axis represent $1''$ intervals. The white bar corresponds to two scans where the telescope was significantly off-pointed, such that no co-aligned data could be recovered. Each time step of 58 s is outlined in black and the overall temporal interval covered is ~ 39 minutes. Note that the horizontal axis has been compressed to show a larger number of frames.

note several features that appear in the CO line core but *not* the three atomic lines. First, we note the existence of several extended ($\sim 10 - 20''$), dark regions to the north of the active region, with the strongest being to the north-east of the pore. While there is a visual similarity between these features and the “thermal shadows” seen by Ayres (1998) in the vicinity of a sunspot pair (see his Figure 5), we note that these regions are confined to the northern edge of the field-of-view. This region is poorly illuminated on the detector, making measurements of the CO line-core intensity there more susceptible to errors in the flat-field correction. Combined with the fact that these features rarely persist between consecutive scans, we believe that these regions of anomalously low intensity are most likely an artifact of the data reduction process. Second, we note that a bright “ring” is visible just surrounding the pore. Something similar is faintly visible in the Na I D1 image, but not in either the Fe I or Ca II images. This suggests that the source of this feature lies between the regions of sensitivity of these two latter lines (i.e. in the upper photosphere or low chromosphere). Lastly, we observe a small, dark region to the southwest of the pore which is about $5''$ in diameter. A space-time diagram of the brightness of this feature (Figure 4) shows this feature displays both a depression of the CO line core intensity and an increase in its equivalent width, and that these changes are long-lived. A similar space-time diagram of its equivalent width (top panel) shows that the decrease in line core intensity corresponds to a simultaneous increase in CO column density. We will describe this feature and those like it as “cold bubbles”, as they appear like isolated pockets of cold, CO-rich gas in the solar atmosphere.

4.2. Epoch Analysis of Cold Bubbles

For the purposes of this paper, we define a “cold bubble” to be a region which displays at least a 2σ enhancement in its CO equivalent width for five or more consecutive NAC scans (approximately 5 min). This technique allows for the detection of persistent features with significant amounts of CO relative to the solar background. During the observing sequence, seven such features were detected (shown in Figure 5). Note that these features are not isotropically distributed across the solar surface. Instead, most of them are clustered around the boundary of the pore; only two are located in what might be considered quiet Sun (despite covering $\sim 90\%$ of the field-of-view). To assess the evolution of these features, we performed an *epoch analysis* of their evolution. As a proxy of the total amount of excess CO in each bubble, we calculated the area-integrated equivalent width within its boundary (defined by the contours shown in Figure 5) in each scan. The resulting curves (one of which is shown in the right panel of Figure 5) were then fit to

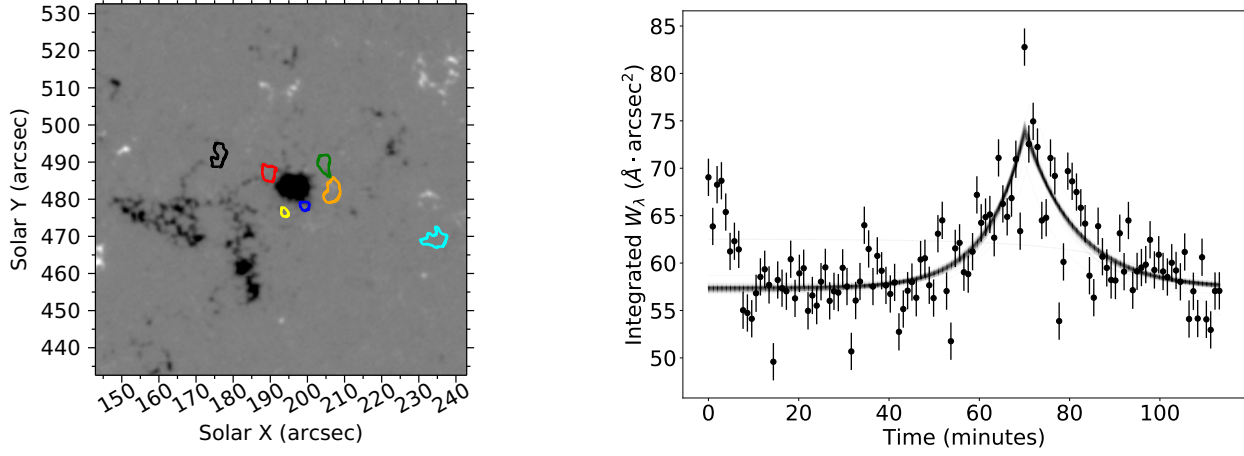


Figure 5. Locations of the seven detected cold bubbles, shown in relation to the HMI magnetogram from Figure 3 (left). A plot of the total equivalent width in one bubble (right), with sample MCMC model curves shown in black. Error bars indicate the uncertainty in each measurement of the integrated equivalent width, propagated from the uncertainty in the CO spectral profile.

an exponential model curve⁴:

$$W_{tot}(t) = W_0 + A \times \begin{cases} 2^{(t-t_0)/\tau_+} & t < t_0 \\ 2^{-(t-t_0)/\tau_-} & t > t_0 \end{cases} \quad (4)$$

where W_0 represents a constant “background” equivalent width, A is the amplitude of the excess signal, t_0 is the time where the signal peaks, and τ_{\pm} are the doubling time (for the rise phase) and the half-life (for the decay phase) of the bubble, respectively. These four model parameters were calculated for each bubble using a Markov-chain Monte Carlo (MCMC) process to ensure convergence to a global minimum solution. These parameters were then used to combine the eight individual curves into a single *epoch curve*, defined to have unit amplitude and to peak at $t = 0$. The epoch curve was fit the same model to estimate characteristic values of τ_{\pm} that describe the collective behavior of the bubbles (see Figure 6 for the results of this analysis).

We note that our model does not aim to describe the small-scale variations of the individual equivalent width curves (such as the effect of the 5-minute oscillations) which leads to a large amount of scatter in the epoch data set which cannot be explained by the propagated uncertainty in the equivalent width measurements. Therefore, fitting the simplified model given by Equation 4 to this data produces a solution with an undesirably large goodness-of-fit metric ($\chi^2 = 23$). The scale separation between the unmodeled effects and the long-term evolution of the bubble ensures that the best-fit model parameters should not be biased by this non-random error – however, the MCMC parameter uncertainties returned by such an approach would be underestimated. Therefore, we chose to artificially scale the uncertainties used in the calculation of the MCMC χ^2 objective function such that the best fit model has $\chi^2 = 1$, in order to retrieve more appropriate model uncertainties for the epoch curve parameters.

Examining the epoch curve (the left panel of Figure 6, we note that the seven normalized bubble curves fit together well into a cohesive exponential profile – justifying our choice of a self-similar model – and that they appear to be well described by the ensemble of MCMC model fits. Examining the bivariate distribution of τ_+ and τ_- (right panel), we see that the estimates of these two parameters are uncorrelated (i.e. independent), with values of $\tau_+ = 8.4^{+1.8}_{-1.5}$ min and $\tau_- = 9.6^{+2.3}_{-1.7}$ min, respectively.

4.3. Comparison of Velocity Power Spectra

In addition to showing different features in their line core intensities, these spectral diagnostics show varying signatures of acoustic wave propagation in their Doppler velocity signals, shown in Figures 7 (for the 5-minute band,

⁴ This model was chosen as the simplest self-similar model for the observed behavior, since self-similarity is implicitly assumed during the re-normalization step of the analysis. Physically, this can be interpreted as a manifestation of self-catalytic CO formation (the “molecular cooling catastrophes” of Ayres & Rabin (1996)).

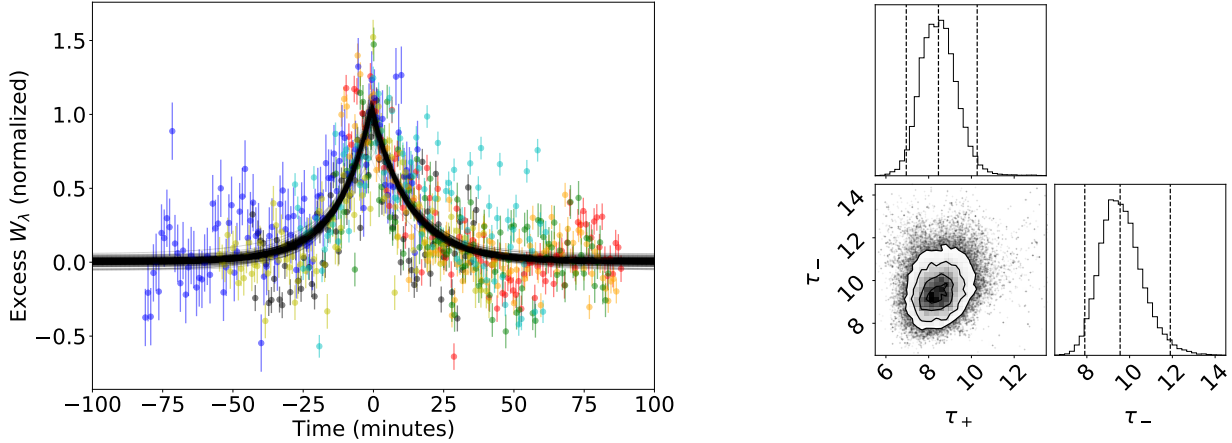


Figure 6. Results of an epoch analysis of the “cold bubble” evolution. *Left panel:* a plot of the normalized, co-aligned excess equivalent width seen in each “bubble” (dots, color coded to match the “bubble” contours seen in Figure 5). Error bars denote the 2σ uncertainty in each measurement, propagated from the uncertainty in the measured CO spectral profiles. Black lines show a sample of MCMC model fits to the data. *Right panel:* a corner plot showing the covariance of the estimates for τ_+ and τ_- . The solid contours in the scatterplot represent the 68%, 95%, and 99% confidence intervals for the bivariate distribution. The top and right plots show the univariate distributions for τ_+ and τ_- , where the dashed lines show the median and 95% confidence intervals for each distribution.

corresponding to photospheric helioseismic oscillations) and 8 (for the 3-minute band, corresponding to frequencies above the acoustic cutoff). In the lines that are sensitive to the lower layers of the solar atmosphere (Fe I 7090 Å and Na I D1), the 5-minute power is roughly isotropic across the field of view, except for a slight depression around the pore and plage. In Ca II 8542 Å, which forms above the height where low-frequency acoustic waves are reflected, the 5-minute power is enhanced in the plage relative to the quiet Sun.

The differences in the 3-minute power are more pronounced; while isotropic in the quiet Sun regions of the field-of-view, there is a region of depressed power (termed the “magnetic shadow” by Vecchio et al. (2009)) surrounding the pore and plage. The size of this region varies between the lines: it is nearly non-existent in the low-forming Fe I line, larger in the intermediate Na I D1, and largest in the high-forming Ca II line. In Ca II 8542 Å, the shadow coincides with the area covered by fibrils in the line core intensity (compare to Figure 3). Additionally, we note that the shadow in Na I D1 may be slightly weaker in the region between the pore and plage (southeast of the pore).

Spatial variations in the CO velocity power are harder to discern due to the poorer spatial resolution and seeing conditions of the NAC observations. However, a few similarities with the IBIS power maps can be found. In maps of the 5-minute power, the CO observations seem most similar to the Fe I and Na I power maps, with a fairly isotropic pattern of power in the quiet Sun (however, unlike in those lines there is not apparent depression in the portion of plage that is visible in the CO scans). A magnetic shadow can also be seen surrounding the pore in the CO 3-minute power map, although it is more tenuous than in the IBIS lines (perhaps simply due to the poorer quality of the CO observing sequence). However, we note that it shows a similar anisotropy to the Na I D1 shadow, showing a lesser depression (or perhaps no depression) of acoustic power to the southeast between the pore and the plage.

Additionally, we calculated the Fourier *phase spectra* of these lines, shown in Figure 9. Examining the phase difference between Na I D1 (left) and Ca II 8542 Å (center) relative to Fe I 7090 Å as a function of frequency, we see two distinct regions. First, at lower frequencies ($\sim 2 - 5$ mHz), the phase curve is flat, and the phase difference between the lines is near zero. At higher frequencies, ($\sim 5 - 8$ mHz) the phase difference increases approximately linearly with frequency. The phase spectrum between Fe I 7090 Å and CO 3-2 R 14 (right) is broader, likely due to seeing-induced decoherence of the velocity trends. However, a slight upturn in the phase spectrum can be seen starting at around ~ 5 mHz, indicating the same sort of behavior as seen in the Na I and Ca II phase spectra. This feature is accentuated by comparing the right panel of Figure 9 with Figure 10, which shows the phase difference between Na I D1 and CO 3-2 R 14. We note that that spectrum is much flatter, perhaps with a slight negative slope above the acoustic cutoff.

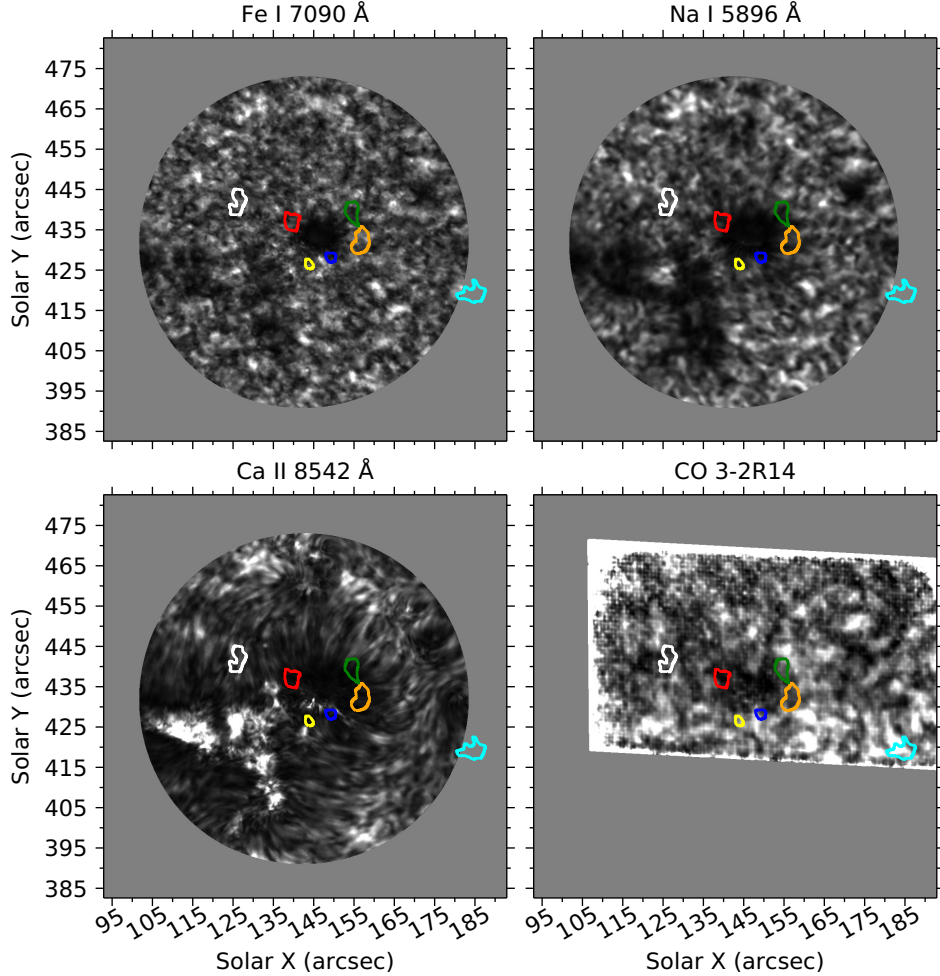


Figure 7. Maps of the 5-minute (3.5 mHz – 5.5 mHz; top row) power in the Doppler velocity of each spectral line. The 5-minute band corresponds to the dominant helioseismic oscillations in the photosphere. The colored contours show the locations of the eight “cold bubbles”.

The appearance of these phase spectra will be explained in Section 5.3.1, where we will use them to estimate the relative formation heights of these lines.

5. DISCUSSION

5.1. Comparison of Diagnostics

While similarities can be found between the CO spectra and various features of the Fe I 7090 Å, Na I 5896 Å, and Ca II 8542 Å lines, the CO 3-2 R 14 line shows several unique features that justify the 4.7 μm band as a spectral region worthy of study in addition to traditional diagnostics of the photosphere and chromosphere.

First, the region surrounding the pore shows a bright ring corresponding to an area with an increased brightness temperature of $T_b \approx 4500$ K. This feature is not seen in observations of fully developed sunspots (see, e.g., Uitenbroek et al. 1994; Ayres 1998), suggesting that its presence may be related to the ongoing decay of this active region. The elevated temperature of this region may indicate a source of heating at the boundary of the pore, such as Joule heating or the dissipation of MHD waves (Stangalini et al. 2021).

Lastly, the CO lines show several long-lived, transient episodes of excess absorption we have termed “cold bubbles”. These events, which may last as long as 30 – 40min, are characterized by diminished brightness temperature and increased equivalent width (i.e. column mass) relative to the quiet Sun in an area as large as 5'' in diameter. This paper marks the first study of such features, which have been largely overlooked in previous studies. Sparse references to unexplained “cooling events” (lasting up to 10 min) in the quiet Sun have been reported (e.g. Ayres & Rabin 1996),

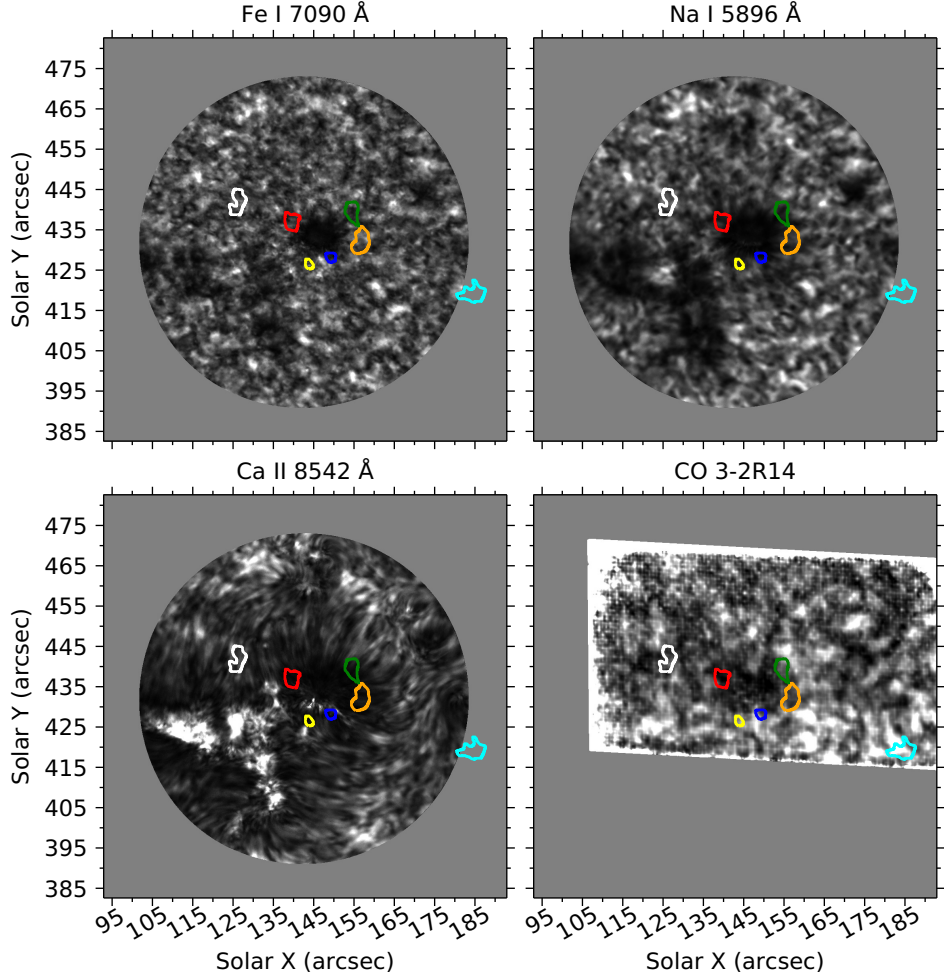


Figure 8. Maps of the 3-minute ($5.7 \text{ mHz} - 7.7 \text{ mHz}$; bottom row) power in the Doppler velocity of each spectral line. The 3-minute band measures the power in frequencies just above the acoustic cutoff $\omega_c \approx 5.5 \text{ mHz}$. The colored contours show the locations of the eight “cold bubbles”.

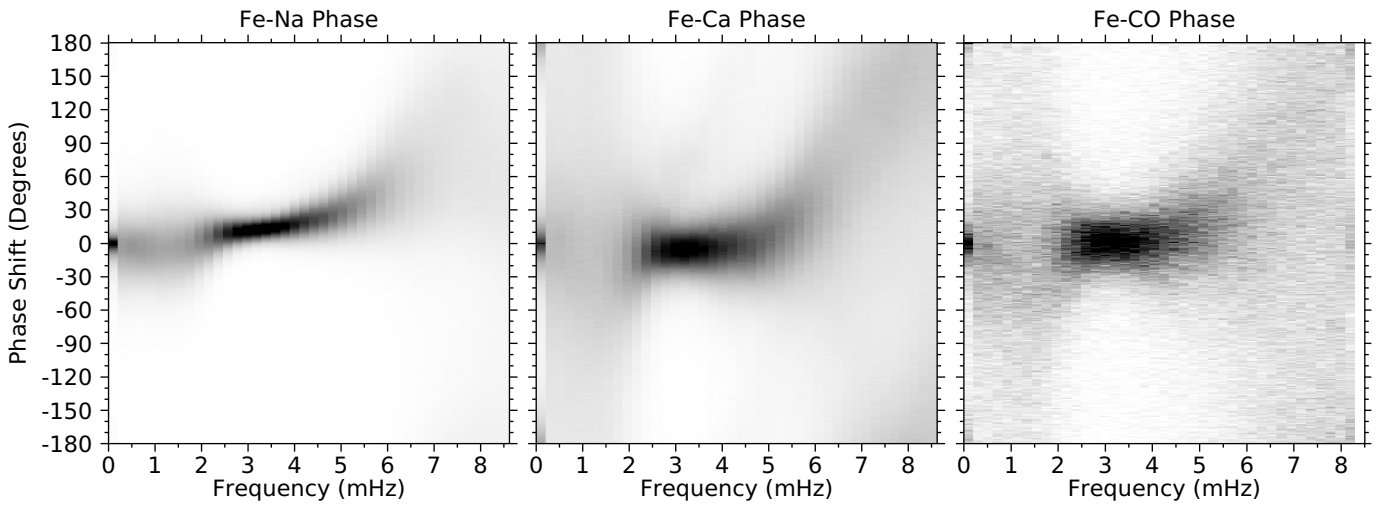


Figure 9. Doppler velocity phase spectra of Na I 5896 Å (left) Ca II 8542 Å (center), and CO 3-2 R 14 (right) with respect to Fe I 7090 Å. Each column represents a histogram of observed phase shifts between Fe I and the listed line for oscillations in a given Fourier frequency bin.

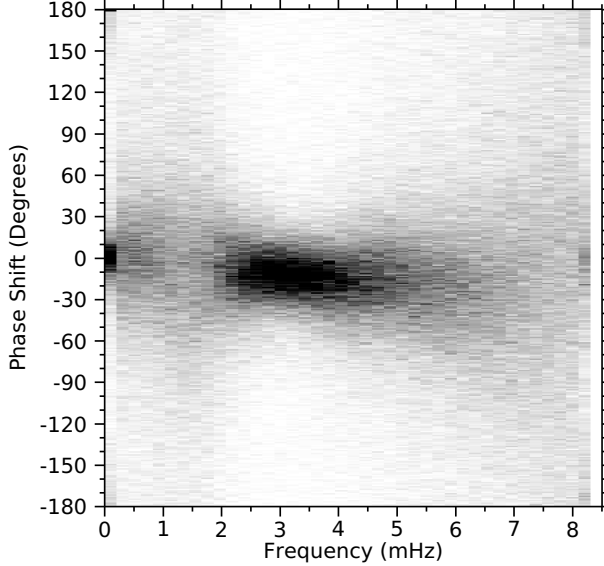


Figure 10. Doppler velocity phase spectra between Na I 5896 Å and CO 3-2 R 14.

but no events of the magnitude or longevity seen here have been reported. It is possible that these two phenomena may be related (e.g. that the cooling events observed by Ayres & Rabin (1996) are short-lived, quiet-Sun analogues of the “cold bubbles” analyzed here). The few studies of CO around magnetic active regions (e.g. Ayres 1998; Uitenbroek 2000) did not report seeing any such transient cooling events, likely because they lacked the temporal resolution to observe the evolution of these features. More recently, preliminary observations of the CO 4.7 μm spectrum by GST/CYRA showed several “unusual absorption features” in the vicinity of a solar pore and its surrounding plage. We believe that these may be examples of “cold bubbles”, although it is not possible to tell for sure from the single raster scan presented by the authors. This phenomenon will be discussed in more detail in Section 5.2.

5.2. Cold Bubbles

First, we must address whether the “cold bubbles” described in Section 4.1 can be explained by phenomena already seen in the literature. In a study of the quiet Sun, Uitenbroek (2000) found that the variation of the CO brightness temperature could be decomposed into two components: (1) the 5” helioseismic oscillations (which act on spatial scales of several arcseconds, but at timescales much shorter than observed here), and (2) the solar granulation (which evolves on a timescale of ∼ 10 min, but on spatial scales that are not resolved by McMP/NAC except in excellent seeing conditions). The scale separation between these processes and the observed spatio-temporal scales of the “cold bubbles” means that the bubbles cannot be easily explained by these phenomena. Supporting this conclusion, we note that both the 5” oscillations and the solar granulation are ubiquitous in the photosphere – meaning that if they directly caused the “cold bubbles”, we would expect to see bubbles occur uniformly within the field of view. The fact that these features instead appear almost exclusively around the pore (despite it filling only a small portion of the target region) suggests that these features may originate in the chromosphere, where the magnetic field can more substantially influence the atmosphere and serve to differentiate the region surrounding the pore from the rest of the quiet Sun.

This hypothesis is supported by examining the evolution timescales τ_{\pm} of the bubbles (obtained through the epoch analysis performed in Section 4.2) to the chemical evolution of CO in the solar atmosphere. If we assume that the formation of these bubbles is mediated primarily by chemical processes, we can equate the measured values of τ_{\pm} with the chemical formation timescale of CO (Ayres & Rabin 1996), which scales with the temperature T and neutral hydrogen density n_H of the solar atmosphere:

$$t_{CO}^{chem} \approx 0.5 \left(\frac{T}{5000 \text{ K}} \right)^{-16.2} \left(\frac{n_H}{10^{15} \text{ cm}^{-3}} \right)^{-1} \text{ sec} \quad (5)$$

Assuming a nominal temperature of 4000 K (the approximate temperature of the cold bubble in Figure 3, obtained from ME inversion) and assuming a timescale of 7 min (on the lower end of our confidence intervals), we can estimate

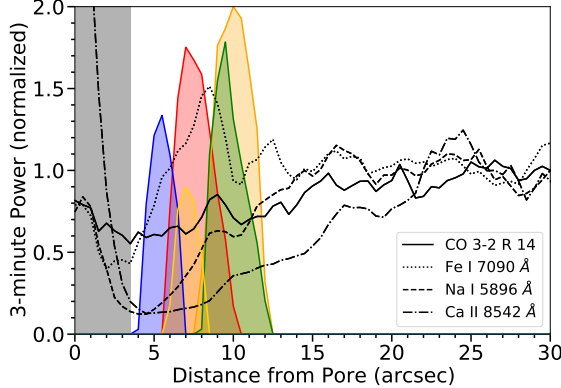


Figure 11. The radially averaged 3-minute power surrounding the pore observed in CO (black), Fe I 7090 Å (red), Na I 5896 Å (blue), and Ca II 8542 Å (orange). All four curves have been normalized to the average quiet-Sun power. The grey shaded region represents the extent of the pore, while the colored shaded regions show the locations of the five bubbles surrounding the pore (color coded to match Figure 5. Taller/wider peaks correspond to larger “bubbles”.

the density of the solar atmosphere in the vicinity of the “cold bubbles” to be about $n_H \approx 4.4 \times 10^{13} \text{ cm}^{-3}$. In the FAL-C atmosphere (Fontenla et al. 1993), this corresponds to a height of $z \approx 970 \text{ km}$ above the $\tau_{500} = 1$ surface of the photosphere, consistent with differential measurements of the CO line core extension relative to the 4.7 μm continuum. We note that this is a lower bound on the bubble’s height in the solar atmosphere, since longer timescales indicate lower densities. For example, a timescale of 12 min (the upper end of the range of uncertainties) corresponds to an altitude of 1040 km.⁵

5.3. Power Spectra

With this hypothesis, the “cold bubbles” represent transient episodes of CO-mediated cooling in the low chromosphere. However, because the bubbles only rarely appear far away from the pore, the presence of the pore’s magnetic canopy field is likely necessary for their formation. This is consistent with the findings of CO5BOLD simulations of CO formation in the solar atmosphere (Wedemeyer-Böhm et al. 2006; Wedemeyer-Böhm & Steffen 2007), which found that heating from acoustic shocks in the non-magnetic Sun prevent the formation of significant CO at chromospheric heights, which would be needed to maintain the “thermal bifurcation” of the chromosphere necessary to explain observed CO limb extensions (e.g. Ayres & Rabin 1996).

Therefore, in order to facilitate the formation of high-altitude CO bubbles, the canopy field must inhibit the acoustic heating of the atmosphere surrounding the pore, such as from acoustic shocks. While it is difficult to confidently identify shocks in the region near the pore (since their decreased amplitude makes them difficult to distinguish from non-shocking velocity perturbations), Vecchio et al. (2009) found a correlation between the integrated 3-minute power in Ca II 8542 Å and the summed shock amplitude observed in that line – therefore, we can treat the 3-minute power as a proxy for shock heating around the pore.

As noted in 4.1, a “magnetic shadow” of depressed 3-minute power is seen surrounding the pore in all four spectral lines, appearing larger and stronger in the higher-forming lines, where the field has spread out from the pore and become more inclined. The extent of the shadow in each spectral diagnostic can easily be seen by examining the radially averaged 3-minute power surrounding the pore, as shown in Figure 11. We note that the five “bubbles” that surround the pore (colored shaded regions) lie well within the boundaries of the shadow, where the 3-minute power is only 60 – 70% of its quiet-Sun value in the CO line (and even lower in Na I and Ca II).⁶

5.3.1. Phase Spectra

The slope of the phase spectra displayed in Figure 9 can be understood by considering the source of velocity power at low ($< 5 \text{ mHz}$) and high ($> 5 \text{ mHz}$) frequencies in the solar atmosphere. The sub-5 mHz power comes primarily from

⁵ These height estimates differ slightly based on the atmospheric model being used. For example, the noted timescales imply a range of heights from $\sim 930 - 990 \text{ km}$ using the cooler FAL-A model, and $\sim 1000 - 1070 \text{ km}$ in the hotter FAL-F model.

⁶ We note that the amplitude of the power depression surrounding the pore in the CO line may be underestimated due to the higher noise floor of the CO power spectra and the fact that the 3-minute power band is much closer to the Nyquist limit for the NAC observations than the IBIS sequence.

helioseismic oscillations: resonant wave modes trapped from below by the density gradient in the solar interior and from above by acoustic reflection by the rarefied upper atmosphere. The majority of the power in these frequencies is in standing wave modes, which oscillate in phase at all heights – therefore, the phase spectrum between any two lines should be zero below the acoustic cutoff frequency. Above this frequency, power is instead carried by travelling waves, which results in a linear phase-height trend. Taking the simplified case of a vertically propagating plane wave, the phase difference between the velocity oscillations of at two heights separated by a distance Δz (representing the regions of sensitivity for two different spectral lines) depends on the wavenumber k of the wave:

$$\Delta\phi = k\Delta z \approx \frac{2\pi\nu}{c_s} \Delta z \quad (6)$$

where ν is the wave frequency and the sound speed is c_s . Here, we see that $\Delta\phi \propto \nu$, explaining the linear phase curve above the acoustic cutoff frequency. Solving for Δz , we have

$$\Delta z \approx \frac{\Delta\phi}{\nu} \frac{c_s}{2\pi} \quad (7)$$

Therefore, Δz is directly proportional to the slope of the phase spectrum (measured in radians/Hz). Assuming a nominal sound speed of $c_s = 7 \text{ km s}^{-1}$, we find that $\Delta z = 520 \text{ km}$ for the Na I phase spectrum and $\Delta z \approx 970 \text{ km}$ for the Ca II spectrum. Given the formation height of Fe I 7090 Å is approximately 250 km, we can estimate that Na I D1 and Ca II 8542 Å form at $\sim 770 \text{ km}$ and $\sim 1200 \text{ km}$, respectively – consistent with radiative transfer modeling of these lines.

Unfortunately, the phase spectrum between Fe I and CO is not coherent enough beyond the acoustic cutoff frequency to confidently measure its propagation slope. However, the phase spectrum between Na I and CO (Figure 10) is much flatter, and even sloped slightly negatively above the acoustic cutoff. This suggests that the average formation height of the CO line may be similar to (or slightly lower than) that of Na I D1, although a confident measurement of the Δz between these lines is out of reach. This is somewhat lower than the heights estimated from the epoch analysis in Section 5.2, which may indicate that the “cold bubbles” represent particularly high-forming pockets of CO. With more stable, high-resolution CO observations, we are confident that the measurement of clear phase spectra between the CO lines and coordinated atomic line observations will be possible, and can serve as a way of measuring the formation height of these lines independently of limb extension observations.

6. CONCLUSIONS

In this paper, we presented the first coordinated observations of the CO 4.7 μm ro-vibrational band with traditional visible/IR atomic diagnostics of the upper photosphere and chromosphere at high resolution. These observations targeted a small pore approximately 22° northwest of disk center ($\mu = 0.91$). While sub-optimal seeing conditions and the under-sampling of the CO raster scan obscured any fine structures of the CO line core intensity (such as the reverse granulation observed by Uitenbroek (2000) in quiet Sun observations), the molecular lines showed several features that do not appear in the atomic lines. First, a bright ($\sim 4500 \text{ K}$) ring surrounds the pore, which indicates an unidentified source of atmospheric heating around the edge of the strong magnetic field concentration. As such a feature does not appear in previous studies of stable sunspots in the CO spectrum (e.g. Ayres 1998), this effect may be related to the ongoing decay of this active region.

We additionally calculated the power and phase spectra of all four spectral lines to study the propagation of acoustic waves in the target region. Maps of the integrated velocity power just above the acoustic cutoff showed a region of diminished power surrounding the pore in all four lines, most visible in the chromospheric Ca II line. The phase difference spectra (measured relative to the lowest forming line, Fe I 7090 Å) showed a linear phase-frequency trend above the acoustic cutoff, which could be used to estimate the regions of sensitivity for each line ($z \approx 770 \text{ km}$ for Na I D1 and $z \approx 1200 \text{ km}$ for Ca II). The phase spectrum obtained from CO was insufficient to directly estimate its height in this way – however, the nearly flat phase spectrum between it and Na I D1 suggests that the velocity signal for the strong CO lines may be sensitive to heights similar to that line on average.

The CO line core intensity also showed several long-lived, $\sim 5''$ “cold bubbles” in the vicinity of the pore. These features are characterized by an extended depression in the brightness temperature of the CO line core and a corresponding increase in equivalent width. They show self-similar growth and decay with exponential timescales consistent with chemical formation timescales in the lower chromosphere ($z \approx 1000 \text{ km}$). These height estimates are similar to

those obtained from trans-limb extension measurements (Solanki et al. 1994), but several hundred kilometers higher than the formation height inferred from the Fourier phase spectra. This could indicate a difference in the contribution functions of the line’s core intensity and Doppler velocity (i.e. the two diagnostics are sensitive to different heights) or that the “bubbles” observed around the edge of the pore represent pockets of unusually high-forming CO.

The majority of these “bubbles” appear in a tight ring around the boundary of the pore, which is surrounded by elongated fibrils in the chromosphere, as seen in the high-forming Ca II 8542 Å line. These fibrils indicate the presence of a horizontal canopy field surrounding the pore, which expands outward into the chromosphere before reconnecting with the photospheric network in the surrounding quiet Sun. The presence of this inclined field creates an “acoustic shadow” of reduced dynamical fluctuation and shock formation in which the “bubbles” appear. Since numerical simulations of non-magnetic atmospheres suggest that shock heating of the chromosphere prevents the condensation of significant CO at those heights (e.g., Wedemeyer-Böhm et al. 2006; Wedemeyer-Böhm & Steffen 2007), we hypothesize that the presence of the acoustic shadow surrounding the pore mediates the formation of these features, explaining their relative abundance around the pore compared to the more energetic quiet Sun.

However, the lack of polarimetry in the atomic line observations presented here limit our ability to reconstruct the solar magnetic field in the upper photosphere and chromosphere. Therefore, to truly examine this hypothesis additional data are needed. Although the McMath Piece Solar Telescope was decommissioned in 2018, two new cryogenic spectrographs – DKIST/Cryo-NIRSP and GST/CYRA – have begun observing the CO 4.7 μm spectrum. These two instruments are initially restricted to standalone observations, necessitating their coordination with other solar telescopes to obtain the multi-wavelength, spectropolarimetric data sets needed to study the relationship between the chromospheric canopy field and chromospheric CO.

7. ACKNOWLEDGEMENTS

We thank Claude Plymate and Eric Galayda for obtaining the McMP/NAC data from Kitt Peak Observatory and Tom Schad, Alexandra Tritschler, Mike Bradford, and Doug Gilliam for the acquisition of the DST/IBIS data at Sac Peak Observatory.

REFERENCES

- Ayres, T., Penn, M., Plymate, C., & Keller, C. 2008, in European Solar Physics Meeting, Vol. 12, European Solar Physics Meeting, 2.74
- Ayres, T. R. 1998, in New Eyes to See Inside the Sun and Stars, ed. F.-L. Deubner, J. Christensen-Dalsgaard, & D. Kurtz, Vol. 185, 403
- Ayres, T. R. 2003, in Astronomical Society of the Pacific Conference Series, Vol. 286, Current Theoretical Models and Future High Resolution Solar Observations: Preparing for ATST, ed. A. A. Pevtsov & H. Uitenbroek, 431
- Ayres, T. R., Plymate, C., & Keller, C. U. 2006, ApJS, 165, 618, doi: [10.1086/504847](https://doi.org/10.1086/504847)
- Ayres, T. R., & Rabin, D. 1996, ApJ, 460, 1042, doi: [10.1086/177031](https://doi.org/10.1086/177031)
- Ayres, T. R., & Testerman, L. 1981, ApJ, 245, 1124, doi: [10.1086/158888](https://doi.org/10.1086/158888)
- Ayres, T. R., & Wiedemann, G. R. 1989, ApJ, 338, 1033, doi: [10.1086/167256](https://doi.org/10.1086/167256)
- Carlsson, M., & Stein, R. F. 1995, ApJL, 440, L29, doi: [10.1086/187753](https://doi.org/10.1086/187753)
- . 1997, ApJ, 481, 500, doi: [10.1086/304043](https://doi.org/10.1086/304043)
- Cauzzi, G., Reardon, K. P., Uitenbroek, H., et al. 2008, A&A, 480, 515, doi: [10.1051/0004-6361:20078642](https://doi.org/10.1051/0004-6361:20078642)
- Cavallini, F. 2006, SoPh, 236, 415, doi: [10.1007/s11207-006-0103-8](https://doi.org/10.1007/s11207-006-0103-8)
- Fehlmann, A., Giebink, C., Kuhn, J. R., et al. 2016, in Society of Photo-Optical Instrumentation Engineers (SPIE) Conference Series, Vol. 9908, Ground-based and Airborne Instrumentation for Astronomy VI, ed. C. J. Evans, L. Simard, & H. Takami, 99084D, doi: [10.1117/12.2232218](https://doi.org/10.1117/12.2232218)
- Fontenla, J. M., Avrett, E. H., & Loeser, R. 1993, ApJ, 406, 319, doi: [10.1086/172443](https://doi.org/10.1086/172443)
- Gudiksen, B. V., Carlsson, M., Hansteen, V. H., et al. 2011, A&A, 531, A154, doi: [10.1051/0004-6361/201116520](https://doi.org/10.1051/0004-6361/201116520)
- Jaeggli, S. A., Lin, H., Mickey, D. L., et al. 2010, Mem. Soc. Astron. Italiana, 81, 763
- Kalkofen, W. 2001, ApJ, 557, 376, doi: [10.1086/321638](https://doi.org/10.1086/321638)
- Kurucz, R. L., Furenlid, I., Brault, J., & Testerman, L. 1984, Solar flux atlas from 296 to 1300 nm
- Leenaarts, J., Carlsson, M., Hansteen, V., & Gudiksen, B. V. 2011, A&A, 530, A124, doi: [10.1051/0004-6361/201016392](https://doi.org/10.1051/0004-6361/201016392)

- Leenaarts, J., Rutten, R. J., Reardon, K., Carlsson, M., & Hansteen, V. 2010, ApJ, 709, 1362, doi: [10.1088/0004-637X/709/2/1362](https://doi.org/10.1088/0004-637X/709/2/1362)
- Li, D., Yang, X., Bai, X. Y., et al. 2020, A&A, 642, A231, doi: [10.1051/0004-6361/202039007](https://doi.org/10.1051/0004-6361/202039007)
- Livingston, W., & Wallace, L. 1991, An atlas of the solar spectrum in the infrared from 1850 to 9000 cm⁻¹ (1.1 to 5.4 micrometer)
- Noyes, R. W., & Hall, D. N. B. 1972, in Bulletin of the American Astronomical Society, Vol. 4, 389
- Pesnell, W. D., Thompson, B. J., & Chamberlin, P. C. 2012, SoPh, 275, 3, doi: [10.1007/s11207-011-9841-3](https://doi.org/10.1007/s11207-011-9841-3)
- Reardon, K. P., & Cavallini, F. 2008, A&A, 481, 897, doi: [10.1051/0004-6361:20078473](https://doi.org/10.1051/0004-6361:20078473)
- Scherrer, P. H., Schou, J., Bush, R. I., & Kosovichev, G. 2011, in The Solar Dynamics Observatory, ed. W. D. Pesnell, P. C. Chamberlain, & B. J. Thompson (New York, NY: Springer), 207–227, doi: [10.1007/978-1-4614-3673-7_10](https://doi.org/10.1007/978-1-4614-3673-7_10)
- Solanki, S. K., Livingston, W., & Ayres, T. 1994, Science, 263, 64, doi: [10.1126/science.263.5143.64](https://doi.org/10.1126/science.263.5143.64)
- Stangalini, M., Erdélyi, R., Bocock, C., et al. 2021, Nature Astronomy, doi: [10.1038/s41550-021-01354-8](https://doi.org/10.1038/s41550-021-01354-8)
- Uitenbroek, H. 2000, ApJ, 531, 571, doi: [10.1086/308454](https://doi.org/10.1086/308454)
- Uitenbroek, H., Noyes, R. W., & Rabin, D. 1994, ApJL, 432, L67, doi: [10.1086/187513](https://doi.org/10.1086/187513)
- Vecchio, A., Cauzzi, G., & Reardon, K. P. 2009, A&A, 494, 269, doi: [10.1051/0004-6361:200810694](https://doi.org/10.1051/0004-6361:200810694)
- Wedemeyer-Böhm, S., Kamp, I., Freytag, B., Bruls, J., & Steffen, M. 2006, in Astronomical Society of the Pacific Conference Series, Vol. 354, Solar MHD Theory and Observations: A High Spatial Resolution Perspective, ed. J. Leibacher, R. F. Stein, & H. Uitenbroek, 301
- Wedemeyer-Böhm, S., & Steffen, M. 2007, A&A, 462, L31, doi: [10.1051/0004-6361:20066173](https://doi.org/10.1051/0004-6361:20066173)
- Yang, X., Cao, W., Gorceix, N., et al. 2020, arXiv e-prints, arXiv:2008.11320. <https://arxiv.org/abs/2008.11320>